

Organosilica Nanoparticles with Ordered Trimodal Porosity and Selectively Functionalized Mesopores

Jana Timm* and Roland Marschall

DOI: 10.1002/cite.202100069

 This is an open access article under the terms of the Creative Commons Attribution-NonCommercial-NoDerivs License, which permits use and distribution in any medium, provided the original work is properly cited, the use is non-commercial and no modifications or adaptations are made.



Supporting Information
available online

Dedicated to Prof. Dr. rer. nat. Jürgen Caro on the occasion of his 70th birthday

Selective functionalization of hierarchical porous materials is of outmost importance for many different applications. A major problem of the functionalization arises from the functionalization process itself. A novel gas phase functionalization was used to modify the surface of newly developed inorganic-organic hybrid nanomaterials with hierarchical trimodal porosity, using 3-mercaptopropyltrimethoxysilane (MPTMS). It was found that the functionalization of mesopores of the material is possible, while the micropores of the material stay selectively non-functionalized after oxidation. Interestingly, the initial mesopores of the material are selectively modified, up to a degree that can be reached usually only by co-condensation approaches, which are however difficult to perform on PMO-derived porous materials.

Keywords: Hybrid materials, Mesoporous materials, Surface characteristics, Surface modification

Received: May 18, 2021; *revised:* August 15, 2021; *accepted:* October 12, 2021

1 Introduction

In 1992 the first ordered mesoporous silica (OMS) materials were investigated [1,2]. These OMS exhibit exceptional high specific surface areas due to inner surface areas resulting from the ordered arrangement of mesopores. The mesoporous structure is created by soft-templating, sol-gel processes in which the silica precursor source (mostly alkoxy-silanes) could hydrolyse and condense in alkaline or acidic media around a liquid crystalline phase of a template (so-called true liquid crystal templating mechanism), or the mesophase formation is induced by the addition of an inorganic precursor and the subsequent hydrolysis and condensation of the precursor molecules (so-called cooperative liquid-crystal template mechanism) [3]. The pore size can be tailored by changing the reaction temperature [1, 4–6]. The usage of alkyltrimethylammonium salts in aqueous alkaline media provoke the formation of 2D hexagonal (Mobil Composition of Matter No. 41, MCM-41), 3D cubic (MCM-48) or even lamellar systems (MCM-50) [1,2]. Additionally, non-ionic block-copolymers (like Pluronic® P123 or F127) could be used in the syntheses as templates in acidic media and leading for instance to 2D hexagonal SBA-15 (Santa Barbara Amorphous No.15) or 3D cubic KIT-6 (Korea Advanced Institute of Science and Technology

No. 6) ordered pore systems [6,7]. In all cases the template molecules can be removed via solvent extraction or calcination in air to get the OMS.

The functionalization of OMS with organic compounds is easy and versatile [8–10]. The incorporation of the organic functionalities could be done during the syntheses, where the silica precursor and the organic functional molecules, mostly organosilanes, hydrolyse and condense around the liquid crystalline phase of the template. The main challenge is here the competition of the different silica sources (organosilane/ alkoxy-silane) to hydrolyze, and to form a homogenous distribution with the template. Therefore, the formation of OMS via co-condensation of organosilica and alkoxy-silane is limited to defined values of the ratio organosilane to alkoxy-silane dependent on the reaction parameters. The maximum ratio of this method leads to organic functionalities below 40 % [3]. Another possibility is to functionalize the surface area of the OMS after the extraction of the template molecules. The main problem of this post-synthetic grafting is the relatively low degree of silanol

Jana Timm, Roland Marschall
jana.timm@uni-bayreuth.de
University of Bayreuth, Universitätsstrasse 30, 95447 Bayreuth, Germany.

groups on the surface [11–13] and the resulting low degree of functionalization [3, 14, 15]. Another problem of the post-synthetic grafting is the required excess of dry solvent during syntheses. Therefore, post-synthetic grafting inspired by chemical vapor deposition of the organosilane avoids this problem, and leads to high functionalization degrees with less utilization of chemicals [16]. But the problem with the limitation of the anchorage of organosilanes is still present. The third method to get ordered mesoporous organic-inorganic hybrid materials is the formation of so-called periodic mesoporous organosilica (PMO) [17–19]. These materials exhibit high specific surface area, ordered pore arrangement, and pore walls consisting of organic moieties. The organic moieties were incorporated in the walls because the precursors of the PMO are bisilylated organic molecules. The bisilylated precursor reacts in the same way as organosilanes or alkyoxysilanes in the reaction solution. Therefore, the formation of OMS-analogue materials with almost 100 % organic bridges is possible and leads to the combination of the unique characteristics of OMS and organic functionalities. Furthermore, PMO materials exhibit silanol groups on their surface, so the subsequent functionalization with further organic units is feasible. The chemical surrounding in the pore walls of PMO differs from the characteristics of the OMS pore walls dependent on the organic bridges in the PMO, but in general the organic bridges lead to less hydrophilic pore walls compared to OMS [20, 21]. The functionalisation of such PMO materials is also of great interest due to the various application fields of PMO such as catalysis, separation or sensing [21, 22]. The interest in medical application of PMO materials also raises constantly [23–25]. Therefore, the optimization of the surface characteristics of PMO materials via post-synthetic functionalization is important for tailoring the materials towards applications.

Here, a rapid and very facile synthesis of PMO-related nanoparticles with trimodal ordered pores of three different pore sizes is presented. The pore walls consist of phenylene bridging units ($-\text{O}_3\text{-Si-C}_6\text{H}_4\text{-Si-O}_3-$) with condensed siloxane groups. Furthermore, this material is functionalized via the chemical vapor deposition (CVD) analogue strategy with the organosilane 3-mercaptopropyltrimethoxysilane (MPTMS). The understanding of gas phase functionalization methods is of high importance to create functional materials in an easy way. We performed detailed investigations on the adsorption and anchorage of MPTMS molecules in dependence of the pore size, which could be investigated by the pore volume and the change in the pore size distributions. Additionally, the accessibility of each pore could be probed by further functionalization.

2 Experimental Section

Chemicals: Cetyltrimethylammoniumbromide (CTAB, Merck, 97 %), NaOH (solid, VWR chemicals, 97–100 %),

MPTMS (Sigma-Aldrich, 95 %), H_2O_2 (Fisher Chemical, 30 %), 1,4-bis(triethoxysilyl)benzene (BTEB, Sigma-Aldrich, 96 %), concentrated HCl (Bernd Kraft, 37 %), Ethanol (Bernd Kraft, technical grade), concentrated HNO_3 (Bernd Kraft, 65 %).

2.1 Synthesis

Synthesis of PMO-related inorganic-organic hybrid nanoparticles (sph-NP) was performed inspired by literature-known syntheses [26, 27]. In a typical synthesis 0.2 g CTAB were dissolved in a mixture of 0.7 mL of 2 M NaOH solution and 96 mL of water at 80 °C. Then 1 mL of BTEB was added to the solution under vigorous stirring. The opaque mixture was stirred for 2 h at 80 °C. Afterwards, the mixture was cooled down with ice water. The mixture was centrifuged for 20 min at 9000 rpm. The particles were washed with water, ethanol, and again water using centrifugation (20 min, 9000 rpm). After drying in air, CTAB molecules were removed by refluxing the particles in a mixture of 100 mL ethanol and 2 mL concentrated hydrochloric acid. After extraction the particles were washed with water, ethanol, and again water. The extracted particles were dried in air at 80 °C for 2 days.

Functionalization of NP: NP functionalization with MPTMS and subsequent oxidation proceeds via already published CVD-type gas phase method [16]. In a general synthesis, 0.3 g of sph-NP was filled in a Teflon inlet of a stainless steel autoclave, then 1 mL MPTMS was filled in a small beaker inside the Teflon inlet, and the autoclave was capped. For 1 min argon was flushed through the Teflon vessel. The vessel was transferred to the autoclave and sealed. The autoclave was heated in an oven for at least 48 h at 120 °C. After cooling the white powder was carefully taken out of the Teflon inlet and the autoclave, washed with water, centrifuged (10 min, 8000 rpm) and dried in air ($T = 25\text{ °C}$, 72 h). This product will be abbreviated in the following as sph-NP-SH. Sph-NP-SH was oxidized under stirring in a mixture of 20 mL conc. H_2O_2 solution and 3 mL conc. HNO_3 for 24 h at room temperature. Afterwards, the mixture was centrifuged at 9000 rpm for 20 min and washed with ethanol and water. The colorless solid was dried for at least 48 h in 25 °C on air. This product will be abbreviated in the following as sph-NP- SO_3H .

2.2 Characterization Techniques

Nitrogen physisorption measurements at -196.15 °C and argon physisorption measurements at -185.75 °C were recorded with ASiQ-MP-MP-AG setup (Anton Paar QuantaTec, Boynton Beach, USA). For the argon physisorption measurements a CryoCooler cryostat (Anton Paar QuantaTec, Boynton Beach, USA) was used to ensure a constant temperature of -185.75 °C during the measure-

ment. The samples were degassed for 16 hours at 120 °C in vacuum prior to the measurement. The data analysis was done via software ASiQwin™ (Anton Paar QuantaTec, Boynton Beach, USA). For the pore size distribution the nitrogen physisorption data was fitted with the non-local density functional theory (NLDFT) adsorption kernel for silica surface and cylindrical pores. For the pore size distribution resulting from the argon physisorption data the NLDFT equilibrium kernel for silica surface and cylindrical pores was used. Water vapor isotherms were also recorded with the ASiQ-MP-MP-AG setup (Anton Paar QuantaTec, Boynton beach, USA). The preparation of the samples was the same procedure as mentioned for the nitrogen/argon physisorption measurements. The measurement temperature was 25 °C, and the saturation vapor pressure (p_0) was set to 23.77 Torr.

Elemental analysis (C, H, N, S) was performed with a Unicube from Elementar with sulfanilamide as the standard. Precise quantities of samples between 2–3 mg were placed in a tin boat and sealed prior to the measurement.

Powder X-ray diffraction (PXRD) data was collected using a PANalytical Empyrean diffractometer equipped with a PIXcel3D detector using CuK α radiation.

Diffuse reflectance infrared Fourier transform (DRIFT) spectra were collected using a Bruker alpha II.

UV/vis measurements were carried out in diffuse reflectance collected from 800 to 200 nm (for better clarity data between 250 and 400 nm are shown) with step width of 1 nm on a PerkinElmer Lambda 750 UV/vis-NIR-spectrometer equipped with a PrayingMantis mirror arrangement. Reflection spectra were converted into absorption spectra via Kubelka-Munk formula.

Fluorescence and time-correlated single photon counting (TCSPC) data were measured on a PicoQuant FluoTime 300 spectrometer, equipped with UV-red detector and a sample holder for solid state samples at room temperature. For the steady-state measurements TimeHarp 260N was selected as photon counter and a 300 W xenon lamp (PicoQuant) as excitation source at 266 nm was chosen. For TCSPC measurements PicoHarp 300 was selected as photon counter and a VisUV laser (PicoQuant) at an excitation wavelength of 266 nm was chosen. The decay was fitted with an exponential function to get three different lifetimes (software: EasyTau2 by PicoQuant).

Transmission electron microscopy (TEM) images were recorded with a Zeiss/LEO EM922 Omega operated at 200 kV located at Bavarian Polymer Institute (BPI) KeyLab Electron and Optical microscopy. Prior to each measurement, less than 1 mg of the sample were suspended in 1 mL of ethanol (AcrosOrganics, extra dry, 99.5 %). Then, 4 μ L of the suspension were dropped on a carbon film coated Cu TEM grid (200 Mesh). TEM images were processed using ImageJ.

Scanning electron microscopy (SEM) images were recorded with a Zeiss LEO 1530 at the Bavarian Polymer Institute (BPI) KeyLab Electron and Optical microscopy. An acceleration voltage of 3 kV was set and the working distance was 5.8 mm with an aperture set to 30 μ m.

Solid state NMR measurements were obtained by using a Bruker Avance III HD spectrometer with an external magnetic field of 9.4 T, equipped with an 4 mm double resonance probe, respectively 3.2 mm double resonance probe for sample sph-NP-SO₃H, spinning frequency of the zirconia rotor was 12.5 kHz (¹H, ¹³C) and 10.0 kHz (²⁹Si), excitation pulse 2.5 μ s for ¹H NMR data and 3.5 μ s for ²⁹Si NMR data, relaxation time 1 s (¹H) and 60 s (²⁹Si). All spectra referenced with respect to tetramethylsilane (TMS) using secondary standard adamantane. Further the ¹³C NMR data was obtained using a ramped cross-polarization (CP) experiment with the nutation frequency on the proton channel was varied linearly by 50 %. The corresponding nutation frequency on the ¹³C channel and the contact time were adjusted to 70 kHz and 1 ms. During acquisition proton broadband decoupling was applied using a spinal-64 sequence with a nutation frequency of 70 kHz.

Dynamic light scattering (DLS) and zeta potential measurements were performed with a Particle Analyzer Litesizer 500 (Anton Paar, Germany) at 25 °C. The zeta potential was calculated via Smolouchowski approximation. For each method three measurements were conducted and averaged. Prior to the measurement, a dispersion of 10 mL ultrapure water (2 ppb) and 5 mg of the powder sample was mixed and ultrasonicated for 10 min at 25 °C.

Thermogravimetric analysis was performed in synthetic air flow with a Netzsch Jupiter STA 449C thermobalance coupled with a Netzsch Aeolos QMS 403C quadrupole mass spectrometer for recording gaseous compounds, i.e., H₂O ($m/e = 18$), CO₂ ($m/e = 44$), and SO₂ ($m/e = 64$).

3 Results and Discussion

Spherical phenylene-bridged PMO-type inorganic-organic hybrid nanoparticles (sph-NP) were synthesized with sizes of 100–200 nm. In Fig. 1 the SEM and TEM images of the extracted sph-NP are presented. The spherical shape and

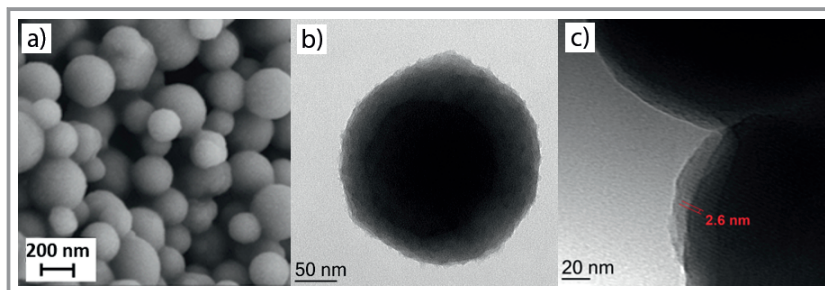


Figure 1. a) and b) Scanning electron and c) transmission electron microscopy images of porous inorganic-organic spherical NP.

the sizes around 100–200 nm are clearly visible in the SEM image (Fig. 1a). Additionally, the TEM image in Fig. 1b shows the uniform spherical shape of the particles, but no templated pores are visible. This wormlike porous structure could be observed earlier for a similar synthesis of spherical PMO NP [28]. The distance between the pore channels (red lines) could only be observed via TEM images with higher magnification (Fig. 1c). The distance between the pore channels could be determined towards 2.6 nm. The morphology, size and the channel distances are comparable to other PMO related nanoparticles, which are bridged via phenylene units [26, 29, 30]. Our rapid and easy approach is also known for the preparation of pure silica MCM-41 nanoparticles; even here the morphology, particle size and channel widths of sph-NP are in good agreement with the pure silica MCM-41 material [27, 28].

Pure silica MCM-41 NP exhibit a 2D hexagonal pore ordering, which can be observed in small-angle X-ray diffraction (SAXRD) patterns [27]. In Fig. 2a the SAXRD pattern of the sph-NP is presented. The maximum of the broad reflection is located at $2.26^\circ 2\theta$. With the assumption of a 2D hexagonal pore arrangement, which is usual for CTAB micelle formation under the present synthesis condi-

tions [2, 17, 27] the pore sizes could be estimated to be 2.3 nm resulting from the distances between the pore centers. The assumption of a 2D hexagonal pore arrangement could be further underlined by channel-like arrangement observed in the TEM images at high magnification (Fig. 1c). The obtained distances of the pore channel of sph-PMO from TEM images (2.6 nm) and SAXRD (2.3 nm) are in good agreement. Powder X-ray diffraction (XRPD) in the wide-angle region shows two major broad reflections. The reflection at $9.8^\circ 2\theta$ could be assigned to a partly periodicity of the phenylene rings in the pore walls with a d spacing of approx. 9 Å. The literature known d spacing is slightly smaller (7.6 Å) [17, 31]. No other reflection according to this signal is present, indicating a low short-range periodicity in the pore walls, similar to KIT-6 PMO [32]. The very broad reflection with a maximum at $23^\circ 2\theta$ can be assigned to the “halo” of amorphous SiO_2 [33–35].

The presence of phenylene bridging units could further confirmed by UV/vis spectroscopy (Fig. 3a). The absorption maxima at 270 and 277 nm could clearly be assigned to aromatic compounds and are in good agreement with the literature [36, 37].

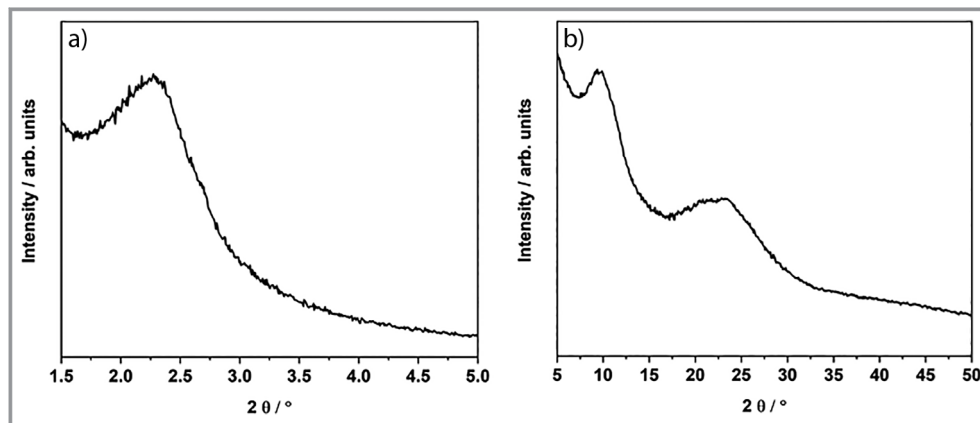


Figure 2. a) Small-angle and b) wide-angle X-ray diffractograms of sph-NP.

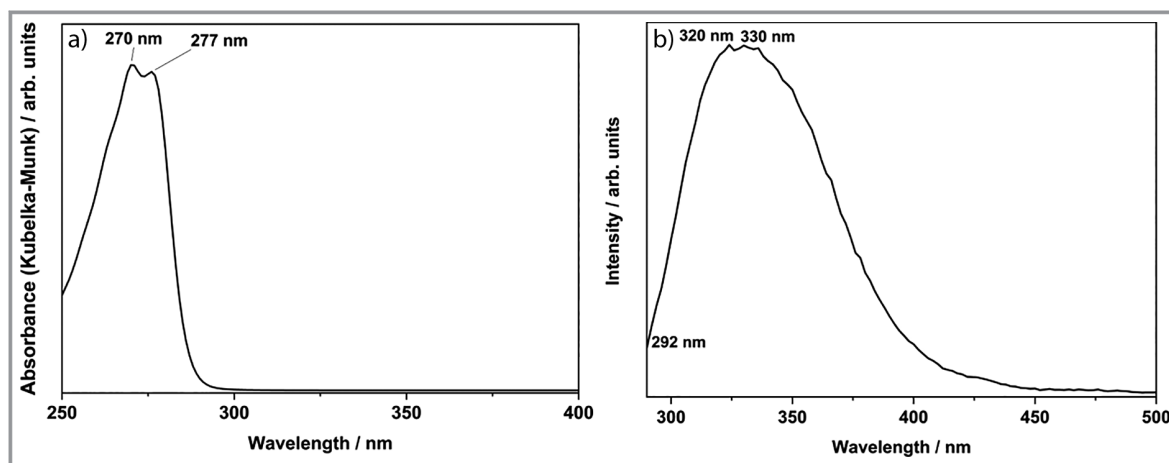


Figure 3. a) UV/vis spectrum of sph-NP and b) fluorescence spectrum of sph-NP excitation wavelength $\lambda_{\text{ex}} = 266$ nm.

The orientation and the ordering of the aromatic rings could be further investigated by photoluminescence (PL) spectroscopy. The maximum in PL corresponds to the degree of ordering of the phenylene units in the PMO material, which was already shown for the PMO with crystalline pore walls in comparison to a PMO with non-crystalline pore walls [38]. For sph-NP a broad maximum in photoluminescence was found in the range between 310–340 nm with signals at around 292 nm (less intense), 320 and 330 nm (Fig. 3b), which is in good agreement to literature and further underlines the partial ordering of the phenylene units in sph-NP [36, 38]. The measured PL lifetimes at 292, 320, and 330 nm (Figs. S1 and S2 in the Supporting Information) are also in the good agreement with literature, showing partial ordering of the phenylene bridging units in the material (Tab. S1) [38].

The porosity of sph-NP and the ordering of the pores was investigated by nitrogen physisorption measurements. In Fig. 4a the nitrogen physisorption isotherm of the sph-NP (black curve) are presented. The isotherm could be classified with type Ib isotherm (IUPAC recommendation [39]), which represents mesoporous materials with mainly small mesopores or wider micropores. A sharp increase in the range of very low p/p_0 values indicates the presence of micropores in sph-NP. The corresponding pore size distribution of sph-NP (Fig. 4b, black curve) shows three different maxima at 0.8, 1.6, and 2.6 nm. The total pore volume is $0.38 \text{ cm}^3 \text{ g}^{-1}$. The specific surface area was calculated with the Brunauer-Emmett-Teller (BET) model [40] plus correction for micropores [41], and a specific surface area of $792 \text{ m}^2 \text{ g}^{-1}$ could be obtained. These values are in good agreement for comparable materials in the literature [28, 29, 42, 43]. Sph-NP were reproduced and comparable isotherms and pore size distributions were obtained (Fig. S3). A trimodal pore size distribution however was not described in the literature so far. The trimodal distribution might be a consequence of a change in the packing parameter of the template molecules. The BTEB precursor first hydrolyses in the reaction mixture and the ethanol concentration in the mixture increases. This concentration change influences the packing parameter g of the template molecule micelles. The formation of wormlike pore arrangement was often explained by this effect [28]. But further the packing parameter g is directly proportional to the micelle volume and therefore might introduce different pore sizes in one material [44–46].

The trimodal pore system of sph-NP is predestined for the investigation of functionalization and diffusion behavior in dependence on the pore sizes. Further the inorganic-organic hybrid pore walls exhibit unique characteristics for such fundamental understandings regarding the functionalization of surfaces with linker molecules like MPTMS. The functionalization method, which we use here, was developed in our group [16] and is a green, solvent-free process. For the deeper understanding of interactions during functionalization procedures this method must be chosen. The

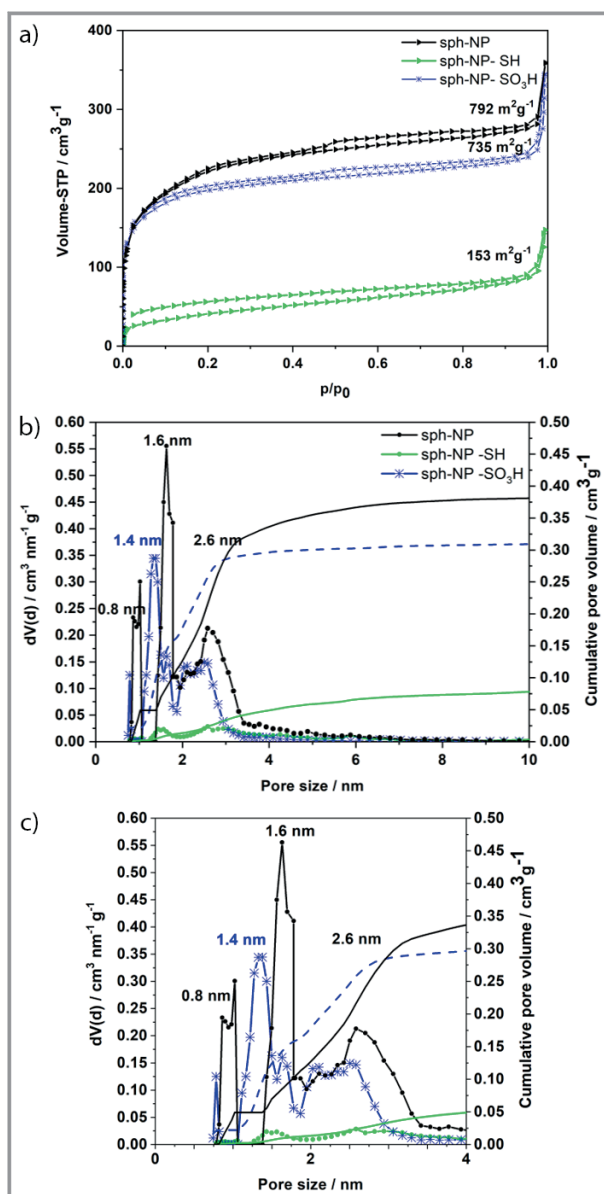


Figure 4. a) Nitrogen physisorption isotherm of sph-NP, sph-NP-SH, and sph-NP-SO₃H at 77 K, b) NLDFT data analysis via adsorption kernel for silica surfaces with cylindrical pores, and c) zoom of the NLDFT data analysis of b).

enormous advantage of the method is that any influence of solvent-linker and solvent-surface interactions are negligible. The only interaction takes place between the linker molecules and the surface and gives therefore detailed information on the surface chemistry. Additionally, the functionalization of the different pores only depends on the pore size and not on effects like capillary condensation or wettability of the solvent. Even the chemical surrounding in the pores of sph-NP is homogenous due to regular attachment pattern of $-\text{O}_3-\text{Si}-\text{C}_6\text{H}_4-\text{Si}-\text{O}_3-$ units. The gas phase functionalization of sph-NP with MPTMS and subsequent

oxidation was therefore investigated by nitrogen physisorption.

The comparison of the nitrogen physisorption isotherms of sph-NP and functionalized sph-NP (sph-NP-SH) clearly shows the influence of the functionalization of the sph-PMO (Fig. 4). The specific surface area decreases by about 90 % (sph-NP-SH: $153 \text{ m}^2 \text{ g}^{-1}$), it seems like the pores become less accessible for gas adsorption due to the functionalization. The subsequent oxidation of the thiol groups with H_2O_2 leads to regained high specific surface areas (sph-NP-SO₃H: $735 \text{ m}^2 \text{ g}^{-1}$), the shape of the respective isotherm can be classified as type I(b) as for mainly microporous materials. This effect of regaining accessible pores could be observed also for OMS materials before [16]. In Fig. 4b and c the pore size distributions (PSD) of the material originating from the NLDFT data analysis are shown. Here the huge differences in the pore volumes of the samples underline further the trend of the values of the surface area. Sph-NP-SH exhibits the lowest pore volume and also less accessible pores. The pore size distribution of the sph-NP-SO₃H shows that the pores are again accessible for gas molecules after oxidation, while the pores with a size of 2.6 nm are affected the most by the surface functionalization with MPTMS, while the other pores with pore sizes of 0.8 and 1.4 nm are regained regarding their amount in the cumulative pore volume. The pore size of 0.8 nm is very close to the size of 0.6–0.7 nm, which single MPTMS molecules occupy as monolayers [47]. Therefore, the functionalization of MPTMS is limited by the small pore size of 0.8 nm/1.4 nm. To exclude interaction of the quadrupole moment of nitrogen and the functionalized surface, we performed argon physisorption measurements at $-186.15 \text{ }^\circ\text{C}$ and found the same trends for non-functionalized and SO₃H-functionalized samples (Fig. S4). The evaluation of the argon physisorption measurements show lower specific surface area (BET method) and slightly smaller pores of the samples. This result could be explained with the high sensitivity of argon towards micropores [48, 49]. To verify the PSD resulting from the gas physisorption measurements, the calculated isotherms of the NLDFT fitting were investigated (Figs. S5 and S6). The filling of the micropores could also be investigated by semi-logarithmic application due to sharp increases in curve shape during micropore filling [48, 49]. In Fig. S7 the nitrogen and argon isotherms are presented in semi-logarithmic application. The micropore filling at low relative pressures is clearly visible for the samples sph-NP and sph-NP-SO₃H. The curve exhibits no sharp rise compared to zeolites [48]. This observation might be explained by the different present pore sizes in the materials. Furthermore, the blocking of all pores directly after the CVD-functionalization could be also explained by the fact that the pores of sph-NP are connected with each other. Therefore, after CVD-functionalization the bigger pores are functionalized and block the entrance of the smaller pores. The concept of targeted pore blocking via post-synthetic functionalization and subsequent unblocking/unlocking of

the pores could be used for introduction of different functionalities in one material [50].

The pore sizes of sph-NP are selectively affected by the functionalization. The reduction of pore size by functionalization with MPTMS is clearly visible by the change in the pore size distribution of the mesopores towards smaller pores, and shows the high covalent anchorage of these molecules on the pore walls of sph-NP even after oxidation. The thermal stability of the samples was investigated via thermogravimetric measurements coupled with mass spectrometry (Fig. S8). The biggest mass loss ($\sim -30\%$) in all samples could be observed at $600 \text{ }^\circ\text{C}$. The mass spectrometry signals at $600 \text{ }^\circ\text{C}$ indicate the thermal degradation of the aromatic rings. In case of sph-NP-SH also a mass loss at $400 \text{ }^\circ\text{C}$ takes place and could be assigned to the degradation of the anchorage of MPTMS molecules. After oxidation the degradation of the propyl chain is shifted towards higher temperature indicating higher thermal stability. This phenomena was described for functionalized mesoporous silica materials [51]. In both cases (sph-NP-SH and sph-NP-SO₃H) the detected mass traces of SO₂ are only less intense. Therefore, the amount of sulphur loading in the samples was analysed by elemental analysis. The results provide sulphur loadings of $6.31\%/1.97 \text{ mmol g}^{-1}$ (sph-NP-SH) and $3.13\%/0.98 \text{ mmol g}^{-1}$ (sph-NP-SO₃H).

The functionalization degree via grafting method/CVD type method is highly influenced by the concentration of the silanol groups on the surface of the support. The concentration of silanol/OH groups on the surface of organosilica materials like sph-NP (OH groups per nm^2 : $\sim 1.1\text{--}1.3$ [31]) is decreased compared to silica material (OH groups per nm^2 : $\sim 1.4\text{--}3$ [20, 52]). The degree of functionalization with -SO₃H is therefore calculated according to the literature [16, 53] and yields in a surface loading of 0.46 sulfonic acid molecules per nm^2 . Taking into account that the MPTMS linker molecules might bind with more than one OH/silanol group, the amount of maximum loading via post-synthetic grafting method is almost achieved here. Thus, a very high loading of propyl-SO₃H chains in the mesopores of the present PMO nanoparticles could be impressively achieved. This result shows only a slightly lower functionalization degree compared to co-condensed periodic mesoporous organosilica [54] and also to SO₃H-modified MCM-41 via co-condensation [27, 55, 56], although being achieved post-synthetically here.

Moreover, the two types of micropores are hardly affected by the functionalization, resulting in selectively modified mesopores by SO₃H-groups. The micropores might still be accessible for other guest molecules like water or others, which might be very interesting for catalytic or proton conduction applications.

To further investigate the effects of the functionalization on the particles, dynamic light scattering (DLS) measurements were conducted. In Fig. 5 the particle size distributions of sph-NP, sph-NP-SH and sph-NP-SO₃H are presented. After the different functionalization steps the

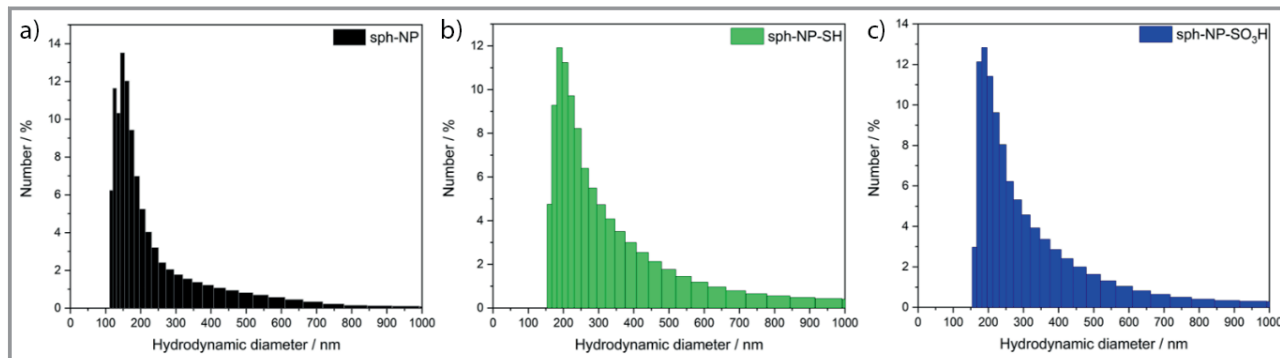


Figure 5. Particle size distribution in ultrapure water of a) sph-NP, b) sph-NP-SH, and c) sph-NP-SO₃H.

maximum in particles size distribution is shifted slightly towards bigger values. The zeta potentials of the materials are -33.71 mV for sph-NP, -33.92 mV for sph-SH, and -41.44 mV for sph-NP-SO₃H. The zeta potential values indicate that hydroxyl groups in sph-NP, the thiol groups in sph-NP-SH and even the sulfonic acid groups in sph-NP-SO₃H are deprotonated under the present conditions [57–59]. Further the zeta potential values show that the dispersion of the sph-NP-SO₃H in ultrapure water is the most stable one compared to sph-NP and sph-SH. This effect could be explained with the high affinity of sulfonic acid/sulfonate [56].

Solid state NMR data further underline the covalent anchorage of MPTMS molecules via CVD process and subsequent oxidation (Fig. 6 and Fig. S9). The signals in the ¹H NMR and ¹³C NMR spectra of all samples (Fig. S9, sph-NP, sph-NP-SH and sph-NP-SO₃H) result from the alkyl and aromatic species of the phenylene-bridged sph-NP as indicated, and agree with literature [17, 32, 51, 60–67]. In the ¹H NMR spectrum of sph-NP-SO₃H the absence of the signals of the alkyl groups is caused by the decreased concentration of propyl chains compared to sph-NP-SH. The integrity of the aromatic bridging units after every synthesis step could be proven by the appearance of only one signal assigned to symmetric bisilylated phenyl rings at 133 ppm in the ¹³C NMR spectra (Fig. S9) and the presence of only T

signals in the ²⁹Si NMR spectra (Fig. 6). After fitting the signals all different functionalities and the phenylene bridged units could be found [16, 26, 51, 62, 63, 65–68]. The integration of the signals of the ²⁹Si NMR of the different samples leads to ratios listed in Tab. S2. The ratio of the T signals in the ²⁹Si NMR spectrum of sph-NP shows the presence of a highly condensed inorganic-organic hybrid material with same OH/OEt groups left for further functionalisation. The values are in good agreement with the literature [26, 62, 63]. During the different functionalisation steps the T³ intensity increases, while the integration leads to smaller values of the T¹ signals of sph-NP. So, the linker molecules are bound covalently to the surface of sph-NP via OH/OEt groups. Additionally, all signals could be assigned to the linker molecules with terminal thiol group or oxidised to the terminal sulfonic acid group. The successful synthesis is further underlined by the absence of T¹ signals for the oxidised sph-NP-SO₃H sample indicating a highly condensed network.

Additionally, the functionalisation of sph-NP is clearly observable via DRIFT spectroscopy. In Fig. 7 the DRIFT spectra of sph-NP, sph-NP-SH, and sph-NP-SO₃H are presented. Most of the vibrations could be attributed to phenylene-bridged silica material [69]. For the non-functionalized sph-NP the Si-OH stretch vibration is very prominent at 3730 cm⁻¹ and underlines the presence of isolated silanol

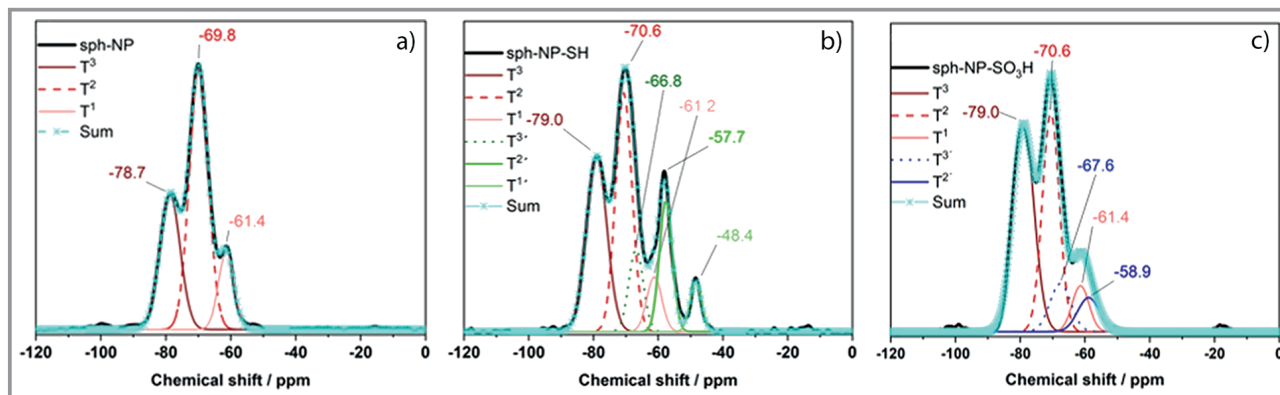


Figure 6. ²⁹Si-NMR spectra of a) sph-NP, b) sph-NP-SH, and c) sph-NP-SO₃H (apostrophe ' indicates signals resulting from the linker molecules (MPTMS or oxidised form)).

groups in the material [20]. After functionalization with MPTMS this vibration is absent and therefore, the covalent anchorage of MPTMS molecules via these silanols groups succeeded quantitatively. The MPTMS molecules in the gas phase are not diffusion-limited by the small pore in sph-NP. Another proof for the successful functionalization is the thiol vibration at 2571 cm^{-1} .

After oxidation the vibration of the thiol group is absent indicating the quantitative reaction with H_2O_2 even in the small pores of sph-NP. The selected view in the region between 1500 and 500 cm^{-1} of the DRIFT spectra makes the oxidation of the thiol groups into SO_3H groups even more clear due to the arising vibrations assigned to sulfonic acid groups (1209 and 1141 cm^{-1}) [70, 71]. The successful oxidation of the thiol groups shows clearly the accessibility of the functionalized pores for a highly polar chemical like H_2O_2 solution. The surface characteristics could also be observed in more detail *via* water vapor isotherms. In Fig. 8 the water vapor isotherms of sph-NP, sph-NP-SH and sph-NP-SO₃H are presented.

The shape of the water vapor isotherms differs considerably. The water vapor adsorption of sph-NP shows S-shape comparable to IUPAC type V isotherm [39]. The low affinity of water adsorption in the low relative pressure (p/p_0) region indicates hydrophobic parts on the surface as expected for the inorganic-organic hybrid [72]. At higher p/p_0 values the adsorption of the water vapor increases due to the water-water interaction and the subsequent filling of the mesopores of sph-NP [73]. The desorption of the water vapor isotherm of sph-NP exhibits a hysteresis loop, which could be explained by the presence of mesopores, and this behavior is in good agreement with an activated carbon material with a high content of oxygen on the surface and comparable pore size distribution [73]. The amount of water vapor uptake for the sph-NP-SH is very low and a small hysteresis is observable in the high p/p_0 region result-

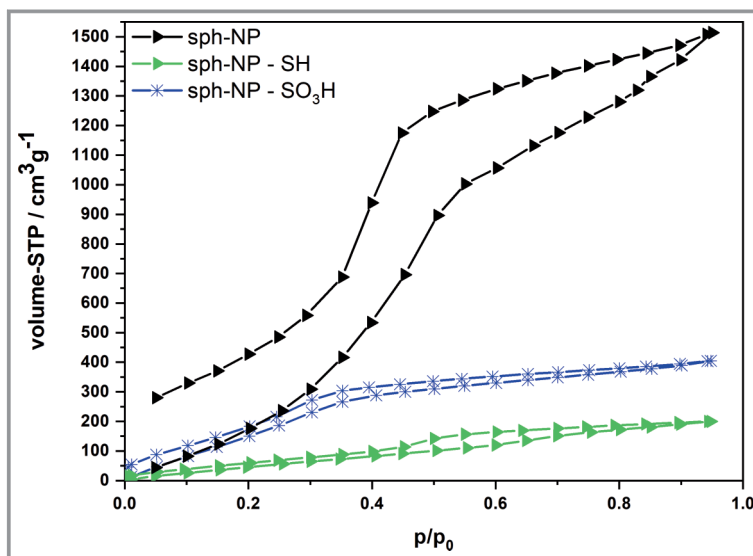


Figure 8. Water vapor physisorption isotherms of sph-NP, sph-NP-SH, sph-NP-SO₃H at 25 °C.

ing from the remaining porosity. The shape of the water vapor isotherm of sph-NP-SO₃H shows a higher water uptake compared to sph-NP-SH, which can be explained with the increasing surface area and increasing bulk hydrophilicity of sph-NP-SO₃H. The amount of adsorbed water up to p/p_0 of 0.3 the values of sph-NP and sph-NP-SO₃H are comparable. So, the water adsorption amount at low p/p_0 values indicates recovery of the surface hydrophilicity after subsequent oxidation of sph-NP-SH. The shape of the adsorption of sph-NP-SO₃H after the sharp increase towards $0.36\ p/p_0$ shows only a slight increase in the adsorbed amount of water vapor. This effect can also be explained with the filling of the residual pores in sph-NP-SO₃H [72, 73]. This S-shaped water vapor isotherm is also often observed in hydrophilic microporous materials like zeolites [74, 75] or metal-organic frameworks (MOFs) [74, 76–78]. This comparison fits well to the data obtained from nitrogen physisorption (Fig. 4).

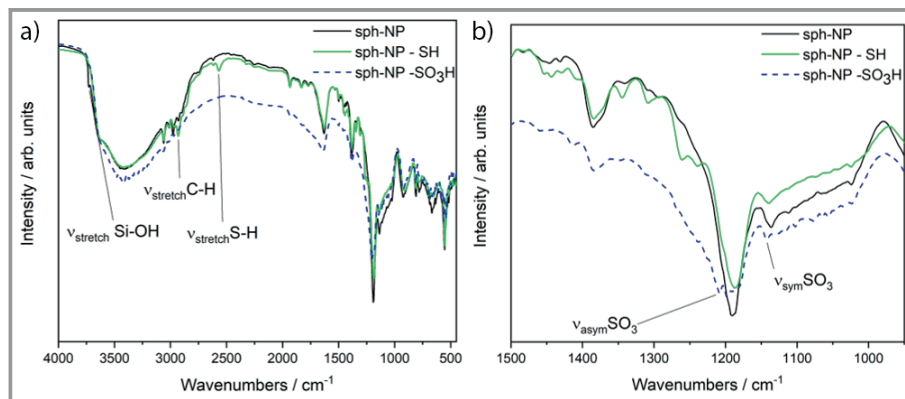


Figure 7. DRIFT spectra a) over the whole range of $4000\text{--}400\text{ cm}^{-1}$ and b) selected view of the region between 1500 and 500 cm^{-1} of sph-NP, sph-NP-SH, and sph-NP-SO₃H.

4 Conclusion

To face the challenge of high functionalization degrees of porous materials with small pore sizes, we successfully performed selective gas phase functionalization of organosilica nanoparticles with trimodal porosity in the mesoporous and microporous range. Our CVD-type approach is able to enable likewise high surface loadings of mesopores as reported by co-condensation routes. Meanwhile, connected micropores were selectively not affected. The choice of porous material with 3 different pore sizes in the range of micropores and also mesopores and medium polar pore walls gives deeper insights in the multi-purpose application of the CVD-type gas phase functionalization. Even if the mesopores of sph-NP-SH seem to be blocked, the accessibility of the pores could be recovered via chemical treatment. This successful chemical treatment further underlines the importance of the versatility of the gas phase functionalization reaction, especially due to the fact that the chemical treatment uses a highly polar substance (H_2O_2) as reagent in highly hydrophobic pore surrounding (phenylene rings in the pore walls plus thiol groups functionalization). The accessibility of small mesopores after functionalization was impressively shown, and the functionalization method creates the opportunity to change material surfaces completely regardless of the initial polarity/hydrophilicity of the surface to be functionalized.

Supporting Information

Supporting Information for this article can be found under DOI: <https://doi.org/10.1002/cite.202100069>. This section includes additional references to primary literature relevant for this research [79].

The authors thank Anja Hofmann for taking SEM images and performing UV/vis measurements, Christopher Simon for taking TEM images (University of Bayreuth), Sabrina Thomä for the help during DLS and zeta potential measurements (University of Bayreuth), Lena Geiling for Thermogravimetric measurements (University of Bayreuth), Anna-Maria Dietel for helping during elemental analysis (University of Bayreuth), Beate Bojer und Prof. Dr. Jürgen Senker for solid state NMR measurements (University of Bayreuth/ North Bavarian NMR center). We thank Rebecca Suckfuell for preliminary experiments. Jana Timm gratefully acknowledges financial support by the Max-Buchner-Research Foundation through a research scholarship (3748).

Abbreviations

BET	Brunauer-Emmett-Teller
BTEB	1,4-bis(triethoxysilyl)benzene
CP	cross-polarization
CTAB	cetyltrimethylammoniumbromide
CVD	chemical vapor deposition
DLS	dynamic light scattering
DRIFT	diffuse reflectance infrared Fourier transform
HCl	hydrochloric acid
HNO ₃	nitric acid
IUPAC	International Union of Pure and Applied Chemistry
KIT-6	Korea Advanced Institute of Science and Technology No. 6
MCM-41	Mobil Composition of Matter
MPTMS	3-mercaptopropyltrimethoxysilane
NaOH	sodium hydroxide
NLDFT	non-local density functional theory
NMR	nuclear magnetic resonance
OMS	ordered mesoporous silica
PL	photoluminescence
PMO	periodic mesoporous organosilica
SAXRD	small-angle X-ray diffraction
SBA-15	Santa Barbara Amorphous No.15
SEM	scanning electron microscopy
TCSPC	time-correlated single photon counting
TEM	transmission electron microscopy
TMS	tetramethylsilane
UV/vis	ultra-violett/visible

References

- [1] C. T. Kresge, M. E. Leonowicz, W. J. Roth, J. C. Vartuli, J. S. Beck, *Nature* **1992**, 359, 710–712.
- [2] J. S. Beck et al., *J. Am. Chem. Soc.* **1992**, 114, 10834–10843.
- [3] F. Hoffmann, M. Cornelius, J. Morell, M. Fröba, *Angew. Chemie Int. Ed.* **2006**, 45, 3216–3251.
- [4] S. O'Brien, R. J. Francis, S. J. Price, D. O'Hare, S. M. Clark, N. Okazaki, K. Kuroda, *J. Chem. Soc., Chem. Commun.* **1995**, 2423–2424.
- [5] O. Trofymuk, A. A. Levchenko, S. H. Tolbert, A. Navrotsky, *Chem. Mater.* **2005**, 17, 3772–3783.
- [6] D. Zhao, J. Feng, Q. Huo, N. Melosh, G. H. Fredrickson, B. F. Chmelka, G. D. Stucky, *Science* **1998**, 279, 548–552.
- [7] T. W. Kim, F. Kleitz, B. Paul, R. Ryoo, *J. Am. Chem. Soc.* **2005**, 127, 7601–7610.
- [8] C. Pirez, J. M. Caderon, J. P. Dacquin, A. F. Lee, K. Wilson, *ACS Catal.* **2012**, 2, 1607–1614.
- [9] F. Goethals, E. Levrau, E. De Canck, M. R. Baklanov, C. Detavernier, I. Van Driessche, P. Van Der Voort, *Materials* **2013**, 6, 570–579.
- [10] Y. K. Seo, S. B. Park, D. Ho Park, *J. Solid State Chem.* **2006**, 179, 1285–1288.
- [11] L. T. Zhuravlev, *Langmuir* **1987**, 3, 316–318.
- [12] L. T. Zhuravlev, *Colloids Surf. A* **2000**, 173, 1–38.
- [13] L. T. Zhuravlev, V. V. Potapov, *Russ. J. Phys. Chem.* **2006**, 80, 1119–1128.

- [14] R. Marschall, I. Bannat, J. Caro, M. Wark, *Microporous Mesoporous Mater.* **2007**, *99*, 190–196.
- [15] M. Wilhelm et al., *J. Memb. Sci.* **2008**, *316*, 164–175.
- [16] J. Timm, R. Marschall, *Adv. Sustain. Syst.* **2018**, *2*, 1700170.
- [17] S. Inagaki, S. Guan, T. Ohsuna, O. Terasaki, *Nature* **2002**, *416*, 45–48.
- [18] C. Vercaemst, P. E. De Jongh, J. D. Meeldijk, B. Goderis, F. Verpoort, P. Van Der Voort, *Chem. Commun.* **2009**, 4052–4054.
- [19] D. Esquivel, O. Van Den Berg, F. J. Romero-Salguero, F. Du Prez, P. Van Der Voort, *Chem. Commun.* **2013**, *49*, 2344–2346.
- [20] M. Ide et al., *Phys. Chem. Chem. Phys.* **2013**, *15*, 642–650.
- [21] W. Wang, J. E. Lofgreen, G. A. Ozin, *Small* **2010**, *6*, 2634–2642.
- [22] N. Mizoshita, T. Tani, S. Inagaki, *Chem. Soc. Rev.* **2011**, *40*, 789–800.
- [23] S. S. Park, M. S. Moorthy, C. S. Ha, *Korean J. Chem. Eng.* **2014**, *31*, 1707–1719.
- [24] J. G. Croissant, X. Cattoën, M. Wong Chi Man, J. O. Durand, N. M. Khashab, *Nanoscale* **2015**, *7*, 20318–20334.
- [25] X. Du, X. Li, L. Xiong, X. Zhang, F. Kleitz, S. Z. Qiao, *Biomaterials* **2016**, *91*, 90–127.
- [26] J. Croissant, X. Cattoën, M. Wong Chi Man, P. Dieudonné, C. Charnay, L. Raehm, J. O. Durand, *Adv. Mater.* **2015**, *27*, 145–149.
- [27] R. Marschall, I. Bannat, A. Feldhoff, L. Wang, G. Q. Lu, M. Wark, *Small* **2009**, *5*, 854–859.
- [28] V. Rebbin, M. Jakubowski, S. Pötz, M. Fröba, *Microporous Mesoporous Mater.* **2004**, *72*, 99–104.
- [29] B. Guan, Y. Cui, Z. Ren, Z. A. Qiao, L. Wang, Y. Liu, Q. Huo, *Nanoscale* **2012**, *4*, 6588–6596.
- [30] N. Knežević, N. Ilić, V. Dokić, R. Petrović, D. Janačković, *ACS Appl. Mater. Interfaces* **2018**, *10*, 20231–20236.
- [31] H. Moon, S. Han, S. L. Scott, *Chem. Sci.* **2020**, *11*, 3702–3712.
- [32] W. Guo, F. Kleitz, K. Cho, R. Ryoo, *J. Mater. Chem.* **2010**, *20*, 8257.
- [33] R. W. G. Wyckoff, *Z. Kristallogr. Cryst. Mater.* **1926**, *63*, 507–537.
- [34] V. Bansal, A. Ahmad, M. Sastry, *J. Am. Chem. Soc.* **2006**, *128*, 14059–14066.
- [35] H. Hamdan, M. N. M. Muhid, S. Endud, E. Listiorini, Z. Ramli, *J. Non. Cryst. Solids* **1997**, *211*, 126–131.
- [36] Y. Goto, N. Mizoshita, O. Ohtani, T. Okada, T. Shimada, T. Tani, S. Inagaki, *Chem. Mater.* **2008**, *20*, 4495–4498.
- [37] J. Timm, A. Bloesser, S. Zhang, C. Scheu, R. Marschall, *Microporous Mesoporous Mater.* **2020**, *293*, 1–8.
- [38] T. Okada, K. Yamanaka, Y. Hirose, Y. Goto, T. Tani, S. Inagaki, *Phys. Chem. Chem. Phys.* **2011**, *13*, 7961.
- [39] M. Thommes, K. Kaneko, A. V. Neimark, J. P. Olivier, F. Rodriguez-Reinoso, J. Rouquerol, K. S. W. Sing, *Pure Appl. Chem.* **2015**, *87*, 1051–1069.
- [40] S. Brunauer, P. H. Emmett, E. Teller, *J. Am. Chem. Soc.* **1938**, *60*, 309–319.
- [41] J. Rouquerol, P. Llewellyn, F. Rouquerol, *Stud. Surf. Sci. Catal.* **2007**, *160*, 49–56.
- [42] J. Croissant, X. Cattoën, M. Wong, C. Man, P. Dieudonné, C. Charnay, L. Raehm, J. Durand, *Adv. Mater.* **2015**, *27*, 145–149.
- [43] M. P. Kapoor, S. Inagaki, *Chem. Lett.* **2004**, *33*, 88–89.
- [44] Y. Zhao, L. Zhao, G. Wang, Y. Han, *Chem. Mater.* **2011**, *23*, 5250–5255.
- [45] J. N. Israelachvili, D. J. Mitchell, B. W. Ninham, *J. Chem. Soc. Faraday Trans. 2 Mol. Chem. Phys.* **1976**, *72*, 1525–1568.
- [46] R. Nagarajan, *Langmuir* **2002**, *18*, 31–38.
- [47] I. Piwoński, J. Grobelny, M. Cichomski, G. Celichowski, J. Rogowski, *Appl. Surf. Sci.* **2005**, *242*, 147–153.
- [48] M. Thommes, K. A. Cychosz, *Adsorption* **2014**, *20*, 233–250.
- [49] K. A. Cychosz, M. Thommes, *Engineering* **2018**, *4*, 559–566.
- [50] M. Kruk, V. Antochshuk, J. R. Matos, L. P. Mercuri, M. Jaronic, K. State, V. Uni, *J. Am. Chem. Soc.* **2002**, *124*, 768–769.
- [51] X. Wang, S. Cheng, J. C. C. Chan, *J. Phys. Chem. C* **2007**, *111*, 2156–2164.
- [52] X. S. Zhao, G. Q. Lu, A. K. Whittaker, G. J. Millar, H. Y. Zhu, *J. Phys. Chem. B* **1997**, *5647*, 6525–6531.
- [53] J. Timm, U. Schürmann, L. Kienle, W. Bensch, *Microporous Mesoporous Mater.* **2016**, *228*, 30–36.
- [54] Q. Yang, M. P. Kapoor, S. Inagaki, *J. Am. Chem. Soc.* **2002**, *124*, 9694–9695.
- [55] R. Marschall, J. Rathousky, M. Wark, *Chem. Mater.* **2007**, *19*, 6401–6407.
- [56] M. Furtmair, J. Timm, R. Marschall, *Microporous Mesoporous Mater.* **2021**, *312*, 110745.
- [57] M. Bouchoucha, R. C.-Gaudreault, M. Fortin, F. Kleitz, *Adv. Funct. Mater.* **2014**, *24*, 5911–5923.
- [58] L. Xiong, X. Du, F. Kleitz, S. Z. Qiao, *Small* **2015**, *11*, 5919–5926.
- [59] S. Sadasivan, D. Khushalani, S. Mann, *J. Mater. Chem.* **2003**, *13*, 1023–1029.
- [60] H. Kao, P. Chiu, G. Jheng, C. Kao, C. Tsai, S. Yau, H. G. Tsai, Y. Chou, *New J. Chem.* **2009**, *33*, 2199–2203.
- [61] M. Bilo, Y. J. Lee, M. Fröba, *Microporous Mesoporous Mater.* **2019**, *284*, 327–335.
- [62] J. Croissant et al., *Chem. Mater.* **2014**, *26*, 7214–7220.
- [63] W. J. Hunk, G. A. Ozin, *Chem. Mater.* **2004**, *16*, 5465–5472.
- [64] R. Siegel, E. Domingues, R. De Sousa, F. Jérôme, C. M. Morais, N. Bion, P. Ferreira, L. Mafra, *J. Mater. Chem.* **2012**, *22*, 7412.
- [65] Q. Yang, M. P. Kapoor, S. Inagaki, N. Shirokura, J. N. Kondo, K. Domen, *J. Mol. Catal. A Chem.* **2005**, *230*, 85–89.
- [66] G. Morales, G. Athens, B. F. Chmelka, R. Van Grieken, J. A. Melero, *J. Catal.* **2008**, *254*, 205–217.
- [67] Z. Xue, H. Shang, C. Xiong, C. Lu, G. An, Z. Zhang, C. Cui, M. Xu, *RSC Adv.* **2017**, *7*, 20300–20308.
- [68] L. Mercier, T. J. Pinnavaia, *Environ. Sci. Technol.* **1998**, *32*, 2749–2754.
- [69] F. Hoffmann, M. Güngerich, P. J. Klar, M. Fröba, *J. Phys. Chem. C* **2007**, *111*, 5648–5660.
- [70] A. Nersasian, P. R. Johnson, *J. Appl. Polym. Sci.* **1965**, *9*, 1653–1668.
- [71] K. Ohno, M. Fukuda, H. Yoshida, H. Tamaoki, H. Matsuura, *J. Mol. Struct.* **2000**, *553*, 49–59.
- [72] J. B. Mietner, F. J. Brieler, Y. J. Lee, M. Fröba, *Angew. Chemie Int. Ed.* **2017**, *56*, 12348–12351.
- [73] L. F. Velasco, R. Guillet-Nicolas, G. Dobos, M. Thommes, P. Lode-wyckx, *Carbon* **2016**, *96*, 753–758.
- [74] H. Kim et al., *Sci. Rep.* **2016**, *6*, 19097.
- [75] C. Anand, Y. Yamaguchi, Z. Liu, S. Ibe, S. P. Elangovan, T. Ishii, T. Ishikawa, A. Endo, T. Okubo, T. Wakihara, *Sci. Rep.* **2016**, *6*, 29210.
- [76] D. Lenzen, J. G. Eggebrecht, P. G. M. Mileo, D. Fröhlich, S. Henninger, C. Atzori, F. Bonino, A. Lieb, G. Maurin, N. Stock, *Chem. Commun.* **2020**, *56*, 9628–9631.
- [77] D. Lenzen et al., *Nat. Commun.* **2019**, *10*, 3025.
- [78] J. Caro, *Chem. Ing. Tech.* **2018**, *90*, 1759–1768.
- [79] Q. K. Loi, T. Horikawa, *Phys. Chem. Chem. Phys.* **2021**, *23*, 12569–12581.